# Zinc Storage Performance of Oxygen-Deficient NH4V3O8: Theoretical and Experimental Study

He Lin *, Xuanxuan Cai , Yu Zhang

Posted Date: 20 February 2024

doi: 10.20944/preprints202402.1113.v1

Keywords: oxygen defects; density functional theory; aqueous zinc-ion batteries; vanadium oxides

*Article*

# Zinc Storage Performance of Oxygen-Deficient $NH_4V_3O_8$: Theoretical and Experimental Study

**He Lin *, Xuanxuan Cai and Yu Zhang**

A State Key Laboratory of Chemistry and Utilization of Carbon Based Energy Resources, School of Chemistry, Xinjiang University, Urumqi Xinjiang, 830017, China; xiaow1456@gmail.com (X.C.); cnuo017@gmail.com (Y.Z.)

* Correspondence: helin@xju.edu.cn (H.L.); Tel.: +86-180-4090-9207 (H.L.)

**Abstract:** Using density functional theory (DFT), the density of states of $NH_4V_3O_8$ (NVO) was analyzed pre and post-oxygen defects ($O_d$) formation. The findings revealed a reduced bandgap in NVO after $O_d$ introduction, emphasizing the role of $O_d$ in enhancing conductivity of the material, thus improving its electrochemical attributes. Through the water bath method, both NVO and its oxygen-deficient counterpart, $(NH_4)_2V_{10}O_{25}\cdot 8H_2O$ ($NVO_d$), were synthesized as potential cathode materials for aqueous zinc-ion batteries (AZIBs). Experimental outcomes resonated with DFT predictions, highlighting the beneficial role of oxygen defects in boosting electrical conductivity. Notably, the refined material displayed a remarkable capacity of 479.3 mAh $g^{-1}$ at 0.1 A $g^{-1}$, underscoring its promise for advanced energy storage solutions.

**Keywords:** oxygen defects; density functional theory; aqueous zinc-ion batteries; vanadium oxides

## 1. Introduction

The escalating energy crisis, exacerbated by a notable scarcity of resources, has catalyzed the advancement of electrochemical energy storage devices. This surge in development is in direct response to the burgeoning demand for diverse sources of renewable and clean energy [1]. A paramount challenge presented by these renewable energy sources is their intrinsic intermittency, which underscores the critical need for efficient energy storage solutions in the lexicon of modern scientific inquiry. In the last decade, lithium-ion batteries (LIBs) have ascended to prominence within this sphere, drawing considerable interest due to their superior energy density and impressive cycle life. Such characteristics have cemented their position as a cornerstone in the field of electrochemical energy storage [2]. Nonetheless, the limited availability of lithium, rising costs, and potential safety hazards associated with the use of organic electrolytes have raised significant concerns [3,4]. This has sparked an increasing interest among the scientific community in investigating alternative battery technologies that promise greater ecological sustainability, cost efficiency, and inherent safety.

In the realm of battery technologies, aqueous zinc-ion batteries (AZIBs) have garnered attention as a promising alternative. Their increasing significance is attributed to a constellation of favorable characteristics, including the abundant availability of zinc resources worldwide, the environmentally friendly nature of zinc utilization, an impressive theoretical specific capacity of 820 mAh $g^{-1}$, and a beneficial redox potential of −0.76 V versus the Standard Hydrogen Electrode (SHE) [5]. Within this context, the cathode material plays a critical role in defining the electrochemical performance of AZIBs. To date, a wide range of cathode materials capable of accommodating $Zn^{2+}$ ions have been investigated. These include manganese oxides (e.g., $MnO_2$, $Mn_2O_3$, $Mn_3O_4$) [6–11], vanadium oxides (e.g., $VO_2$, $V_2O_5$, $Na_2V_6O_{16}\cdot 1.63H_2O$) [12–15], Prussian blue analogs (e.g., $Zn_3[Fe(CN)_6]_2$) [16–18], and a variety of emerging materials [19–23].

Vanadium-based materials, characterized by their multiple valence states and open-framework structures, are regarded as highly promising candidates for cathodes in AZIBs due to their exceptional zinc storage capabilities and excellent cyclability [24,25]. A notable challenge within this domain is the electrostatic interaction between $Zn^{2+}$ ions and vanadium oxide layers, which results in the sluggish migration of $Zn^{2+}$ within the layered matrices. Strategies such as electrostatic shielding

 doi:10.20944/preprints202402.1113.v1



and the expansion of ion diffusion pathways have been demonstrated to effectively mitigate this impediment. Techniques including interlayer metal ion doping (e.g., $Na_{0.33}V_2O_5$, $Li_{0.7}V_6O_{15}$) and the incorporation of structural water ($V_2O_5{\cdot}nH_2O$) are prevalent approaches to addressing these challenges [26]. While the insertion of metal ions as pillars can significantly enhance the ion diffusion channels, it is observed that these heavier ions contribute minimally to the storage of $Zn^{2+}$ [27]. Conversely, employing $NH_4V_3O_8$ (NVO) nanobelts, which utilize lighter $NH_4^+$ ions as structural pillars, has been shown to offer substantial volumetric and gravimetric capacities for AZIB cathodes. The formation of hydrogen bonds between $NH_4^+$ and the VO layers further reinforces the cohesion within the layered structure, promoting structural stability [28–30]. Additionally, the introduction of defects into the crystal lattice, such as oxygen vacancies, has been identified as a potent means of enhancing the performance of AZIBs. These defects can facilitate ion diffusion kinetics and foster more efficient ion intercalation and deintercalation processes, thereby suppressing undesired phase transitions and modifying the material's conductivity [31].

In light of the considerations presented, this study proposes the development of a vanadium ammonium cathode material characterized by a robust layered structure and enriched with oxygen defects ($O_d$) for enhanced performance in AZIBs. Initially, density functional theory (DFT) calculations were employed to investigate the alterations in the density of states for NVO consequent to the induction of $O_d$. The findings from these calculations revealed a reduction in the bandgap of NVO subsequent to the integration of $O_d$. This observation suggests that the presence of $O_d$ within the VO layers modulates the material's internal structure, thereby augmenting its electrical conductivity—a factor that is pivotal for the amelioration of electrochemical performance.

Subsequently, employing a water bath synthesis method, NVO and oxygen-deficient ($(NH_4)_2V_{10}O_{25}{\cdot}8H_2O$ ($NVO_d$) nanosheets were synthesized and evaluated as cathode materials for AZIBs. The congruence between experimental outcomes and theoretical predictions underscores the efficacy of oxygen defects in bolstering the electrical conductivity of the crystal structure. The $NVO_d$ material demonstrated an exemplary capacity, achieving 479.3 mAh $g^{-1}$ at a current density of 0.1 A $g^{-1}$. This evidence firmly establishes the significant role of $O_d$ in enhancing the electrochemical attributes of vanadium-based cathode materials for AZIB applications.

## 2. Results and Discussion

### *2.1. DFT Calculations*

Layered cathode materials are poised to play a pivotal role in the advancement of AZIBs, attributed to their inherent potential for high energy storage capacities. However, the practical application of these materials is significantly hindered by the sluggish diffusion kinetics of $Zn^{2+}$, a phenomenon often precipitated by the structural collapse of the cathode material during electrochemical cycling. In an effort to circumvent this challenge, the strategic integration of $O_d$ within the vanadium oxide (VO) layers has been identified as a promising approach to reinforce structural stability and enhance $Zn^{2+}$ diffusion kinetics.

To rigorously evaluate the impact of $O_d$ incorporation on the structural and electrochemical performance of NVO cathodes, DFT calculations were undertaken. These computational analyses aimed to elucidate the variations in electronic structure of NVO before and after the introduction of $O_d$, and further assess how these oxygen vacancies alter the electronic density of states.

Figure 1a–c delineates the schematic representations of the conventional cell structures for three distinct configurations: the pristine NVO structure, NVO-$O_d$, and the configuration of NVO-$O_d$ subsequent to the incorporation of $Zn^{2+}$ ions (Zn-$NVO_d$). Initially, to ascertain the impact of $O_d$ on the electrical conductivity of these systems, density of states (DOS) calculations were performed. The DOS analysis, illustrated in Figure 1d, reveals that the band gap of pristine NVO is quantified at 1.49 eV. Upon the introduction of $O_d$, there is a significant reduction in the band gap to 0.185 eV, highlighting the enhanced metallic character of NVO-$O_d$ which is indicative of improved conductivity. This enhancement in conductivity is attributed to the structural modifications induced

 doi:10.20944/preprints202402.1113.v1



by the incorporation of $O_d$ into the NVO matrix, which not only facilitates the insertion and extraction of $Zn^{2+}$ ions but also provides additional electrons to augment the capacity.

Subsequent to the embedding of $Zn^{2+}$ into NVO-$O_d$, the band gap is observed to vanish, with the emergence of a new peak at the Fermi level, as depicted in Figure 1e. The projected density of states (PDOS) analysis for the three systems elucidates distinct variations in the state density distributions, particularly around the Fermi level. Notably, the incorporation of $Zn^{2+}$ into NVO-$O_d$ results in the Fermi level being shifted below 0 eV, with discernible states associated with vanadium (V) evident at the Fermi level. The introduction of $O_d$ into the NVO framework notably influences electron transfer processes related to V; the embedding of $Zn^{2+}$ ions transforms the material's character to metallic, thereby enhancing electron mobility within the material. This series of observations underscores the critical role of $O_d$ in modulating the electronic structure and optimizing the electrochemical performance of NVO-based cathodes for aqueous zinc-ion batteries.

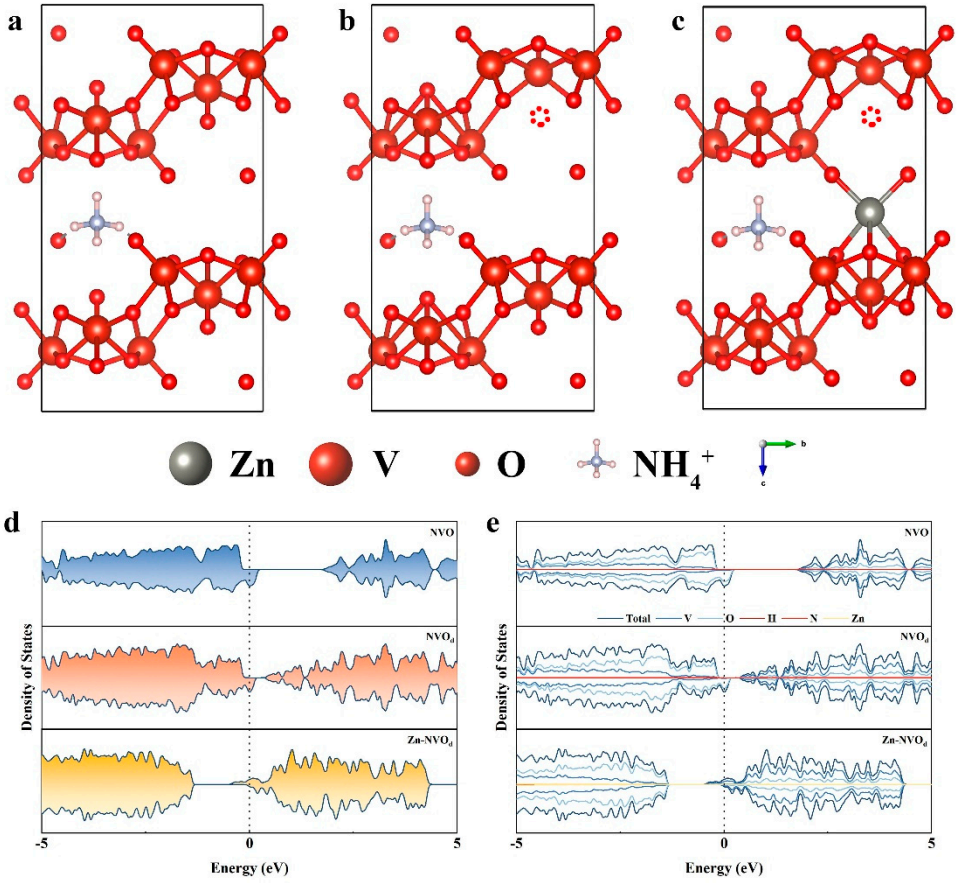


**Figure 1.** Conventional unit cell of (**a**) NVO, (**b**) $NVO_d$ and (**c**) Zn-$NVO_d$ after $Zn^{2+}$ insertion; (**d**) DOS and (**e**) PDOS of the above three structures.

*2.2. Composition and Structural Characterization*

Utilizing the reductive capabilities of thiourea in acidic environments, nanosheets of oxygen-deficient $NVO_d$ were synthesized via a straightforward water bath methodology, employing $NH_4VO_3$ as the starting material. The decomposition of thiourea under heated acidic conditions results in the generation of ammonia, carbon dioxide, and hydrogen sulfide ($H_2S$) gas through a hydrolysis reaction. The evolution of $H_2S$ gas during this process facilitates the introduction of $O_d$ into the forming $NVO_d$, acting as Lewis acid sites. To explore the effect of varying thiourea concentrations, different molar quantities of thiourea (2, 3, and 4 mmol) were utilized, resulting in the synthesis of distinct batches of $NVO_d$, designated as $NVO_d$-2 (with 2 mmol thiourea), $NVO_d$-3 (with 3 mmol

 doi:10.20944/preprints202402.1113.v1



thiourea), and $NVO_d$-4 (with 4 mmol thiourea). For comparative purposes, a control batch of NVO material was also prepared under identical conditions but without the addition of thiourea.

The crystalline structure of the synthesized $(NH_4)_2V_{10}O_{25}\cdot 8H_2O$ was characterized using X-ray diffraction (XRD) analysis. The XRD patterns for the derived $NVO_d$ and $NH_4V_3O_8$ specimens are presented in Figure 2a. Analysis revealed that the diffraction peaks corresponding to $NVO_d$-2, $NVO_d$-3, and $NVO_d$-4 samples align with the (001), (003), (004), (020), and (420) planes, as per the standard Powder Diffraction File (PDF) card for $(NH_4)_2V_{10}O_{25}\cdot 8H_2O$ (JCPDS number: 26-0097), indicating a pure phase of $NVO_d$ with no detectable impurities resulting from the thiourea addition.

A detailed examination of the XRD spectra, particularly around the (001) diffraction peak, is illustrated in Figure 2b. The observed shift of the (001) diffraction peak towards lower angles with an increase in thiourea concentration suggests an expansion in the interlayer spacing of the material. This phenomenon indicates that the introduction of $O_d$ via thiourea not only modifies the internal crystal structure but also induces a structural rearrangement that impacts the interlayer distance, facilitating enhanced electrochemical functionality.

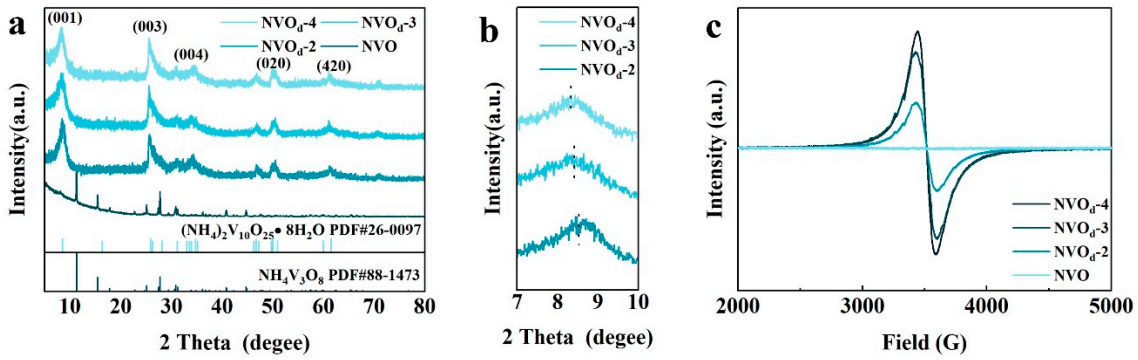


**Figure 2.** (a) XRD patterns of $NVO_d$-2, $NVO_d$-3, $NVO_d$-4 and NVO; (b) Partial XRD patterns of $NVO_d$; (c) EPR spectroscopy of $NVO_d$-2, $NVO_d$-3, $NVO_d$-4 and NVO.

Electron paramagnetic resonance (EPR) spectroscopy was utilized to ascertain the presence of $O_d$ within the synthesized materials, as depicted in Figure 2c. The distinct sharp signal observed in the EPR spectrum of $NVO_d$ can be attributed to electrons localized at defect sites, with the resonance corresponding to a g-value of approximately 2.02, indicative of $O_d$. Notably, the intensity of this signal—and hence the concentration of oxygen vacancies—shows a direct correlation with the quantity of thiourea used during the synthesis process. In stark contrast, samples of NVO prepared in the absence of thiourea exhibited no discernible Lorentzian EPR signals, unequivocally indicating a lack of detectable $O_d$ within these materials. This observation underscores the pivotal role of thiourea as a facilitator of structural transformation, specifically through the induction of oxygen vacancies. Such vacancies are instrumental in modifying the electronic structure and enhancing the functional properties of the material, as evidenced by the pronounced EPR signals in thiourea-treated samples. This finding corroborates the hypothesis that thiourea not only acts as a reducing agent but also as a structural modifier, introducing beneficial defects that can significantly influence the material's electrochemical performance.

The surface morphology of the synthesized materials was meticulously examined using scanning electron microscopy (SEM). Figure 3a–i displays the SEM images of the $NVO_d$ samples with varying degrees of oxygen deficiency ($NVO_d$-2, $NVO_d$-3, and $NVO_d$-4), captured at different magnifications. These images elucidate that the $NVO_d$ samples are composed of irregularly shaped nanosheets, with thicknesses predominantly in the range of 70 to 90 nm. An interesting observation is the morphological evolution observed with increasing $O_d$ content; the materials gradually transition from voluminous nanosheets to more fragmented nanobelts, albeit with the thickness of the structures remaining relatively constant across the samples.

 doi:10.20944/preprints202402.1113.v1



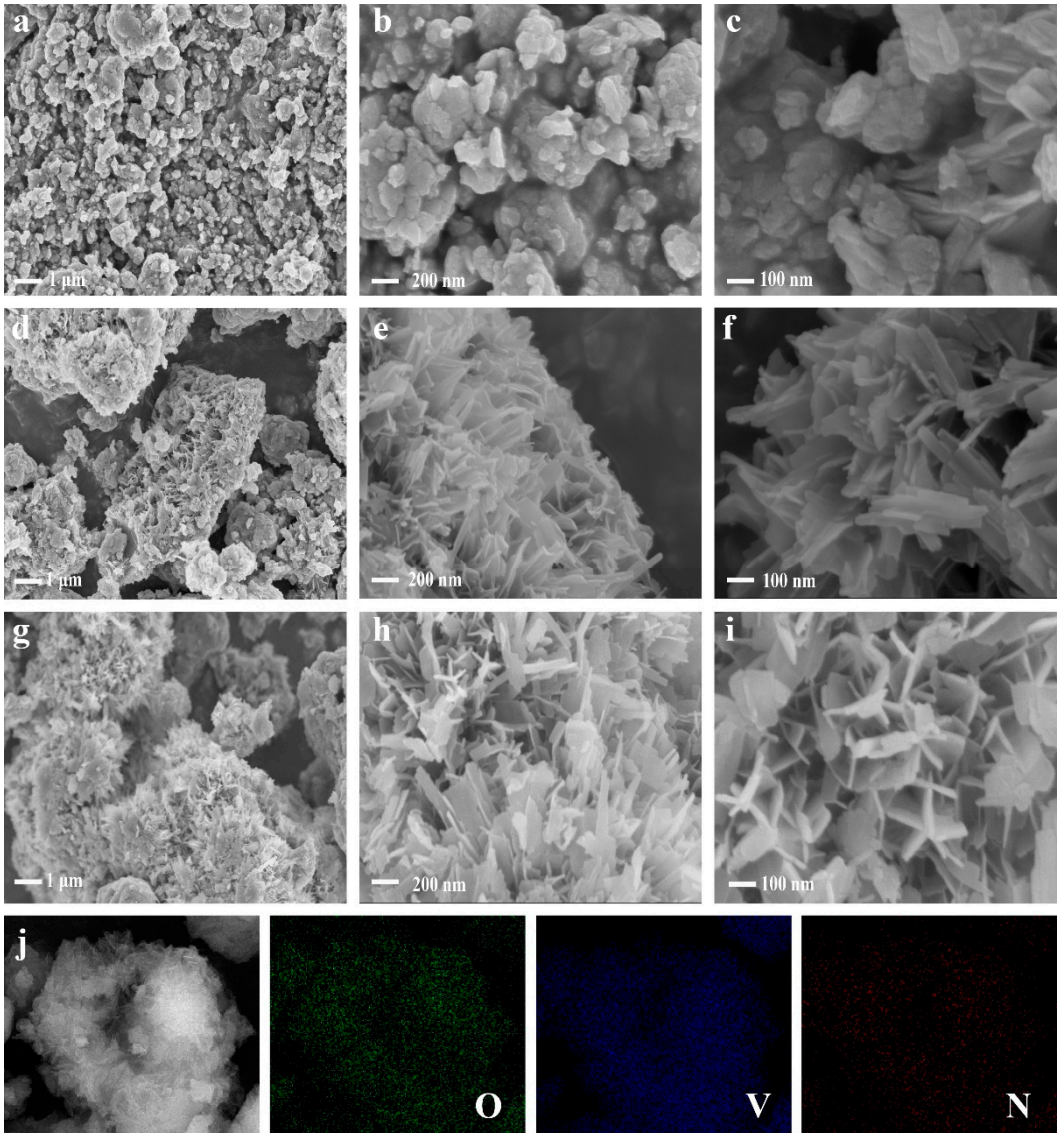


**Figure 3.** SEM images of (a-c) $NVO_d$-2, (d-f) $NVO_d$-3 and (g-i) $NVO_d$-4 at different resolutions; (j) EDS mapping elemental analysis of $NVO_d$-3.

To further elucidate the compositional homogeneity of the synthesized $NVO_d$ nanosheets, energy-dispersive X-ray spectroscopy (EDS) mapping analysis was conducted. The EDS results, illustrated in Figure 3j, confirm the uniform distribution of nitrogen (N), oxygen (O), and V elements across the nanosheets. Notably, sulfur (S) was not detected in the EDS analysis, indicating the effective incorporation of oxygen defects without introducing sulfur impurities into the material. This comprehensive characterization not only confirms the successful synthesis of $NVO_d$ with specific morphological traits but also underscores the homogeneity of elemental distribution, which is crucial for the consistent electrochemical performance of these materials in AZIBs.

The comprehensive X-ray photoelectron spectroscopy (XPS) analysis depicted in Figure 4a confirms the presence of V, O, N, and carbon (C) elements in both NVO and $NVO_d$ samples, with S elements conspicuously absent, as demonstrated in Figure 4b. This observation aligns with the findings obtained from EDS mapping analysis, further corroborating the purity of the synthesized materials. Figure 4c showcases the XPS spectra of the V 2p for both NVO and $NVO_d$-3 samples. The incorporation of oxygen $O_d$ is evidenced by a valence state transition of vanadium, with a partial reduction from $V^{5+}$ to $V^{4+}$. This transition is attributed to the reduction in the number of neighboring oxygen atoms surrounding the vanadium atoms, leading to an increased electron density in the vicinity of V. Such a phenomenon is indicative of the structural modifications within the VO framework prompted by the integration of $O_d$, which not only facilitates the embedding and de-

 doi:10.20944/preprints202402.1113.v1



embedding processes of $Zn^{2+}$ ions but also contributes additional electrons, thereby augmenting the material's capacity.

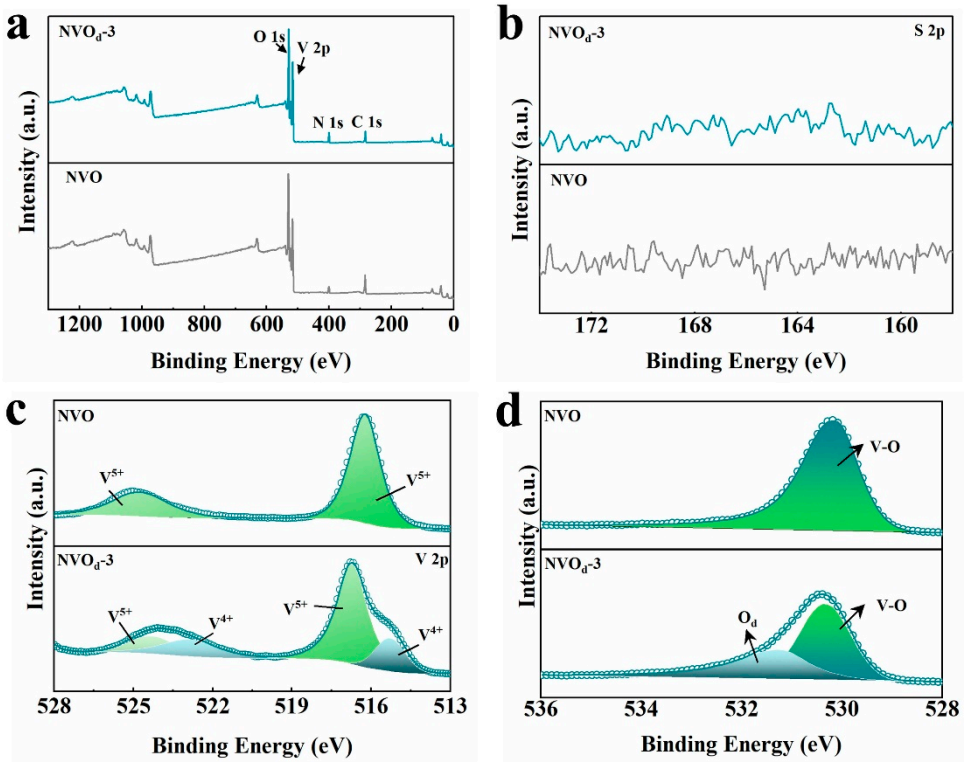


**Figure 4.** (**a**) XPS survey of NVO$_d$-3 and NVO; (**b**) S 2p XPS spectra of NVO$_d$-3 and NVO; (**c**) V 2p XPS spectra of NVO$_d$-3 and NVO; (**d**) O 1s XPS spectra of NVO$_d$-3 and NVO.

Further elucidating the structural and compositional nuances, Figure 4d presents the XPS spectra of the O 1s for both NVO and NVO$_d$-3. The peak associated with lattice oxygen (V-O) in NVO is recorded at 530.18 eV. In contrast, for NVO$_d$-3, this peak shifts slightly to 530.28 eV, with the peak indicative of O$_d$ observed at 531.28 eV. This subtle shift not only confirms the successful introduction of O$_d$ but also highlights the resultant structural rearrangement and its implications on the electronic environment surrounding the V centers.

*2.3. Electrochemical Properties Characterization*

O$_d$ can serve as pivotal contributors to the charge transfer process, offering numerous jump sites and active sites that are instrumental in defining the structural stability of cathode materials. To evaluate the influence of O$_d$ on electrochemical performance, a zinc//NVO$_d$ battery was constructed, utilizing zinc foil as the anode and 3M $Zn(CF_3SO_3)_2$ as the electrolyte. The electrochemical properties of this assembly were subsequently investigated to ascertain the impact of O$_d$ on the battery's performance metrics.

Figure 5a illustrates the specific capacities of the electrode materials NVO$_d$-2, NVO$_d$-3, NVO$_d$-4, and NVO, evaluated at a current density of 0.2 A $g^{-1}$. It is observed that an increase in O$_d$ content correlates with enhancements in both the specific capacity and cycling stability of the electrodes. However, this trend reverses when the O$_d$ content surpasses a certain threshold, leading to a reduction in electrode capacity. This decline in performance, particularly noted for NVO$_d$-4 which demonstrated a capacity of 386 mAh $g^{-1}$ at 0.2 A $g^{-1}$, can be attributed to structural degradation resulting from an overabundance of O$_d$, underscoring the critical balance required in optimizing O$_d$ levels for improved electrochemical performance.

 doi:10.20944/preprints202402.1113.v1



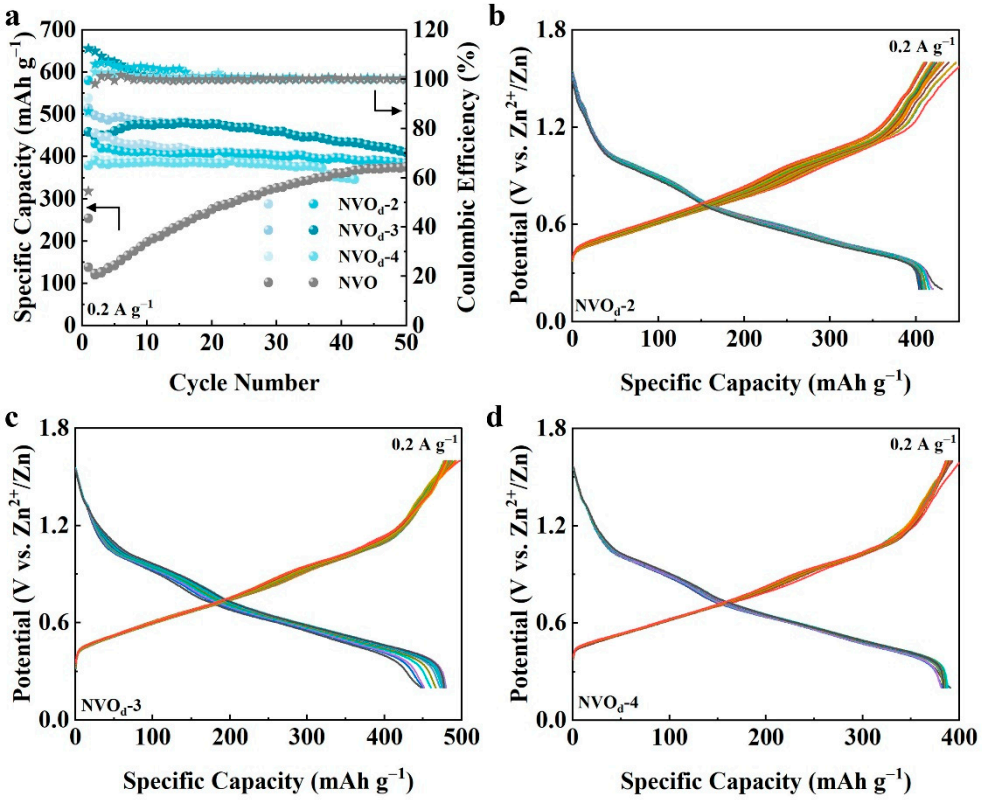


**Figure 5.** (**a**) Cycling performance of NVO$_d$-2, NVO$_d$-3, NVO$_d$-4 and NVO at 0.2 A g$^{-1}$; Galvanostatic charge–discharge profiles of (**b**) NVO$_d$-2, (**c**) NVO$_d$-3 and (**d**) NVO$_d$-4 for the first 20 cycles, correlating with the cycling performance presented in (**a**).

The investigation into the electrochemical behavior of NVO$_d$ materials enriched with O$_d$ reveals a superior performance compared to pristine NVO materials. This enhancement suggests that O$_d$ play a vital role in augmenting the electrochemical attributes of ammonium vanadate-based cathodes. Specifically, the NVO$_d$-3 cathode distinguishes itself by delivering an exceptional initial discharge capacity of over 458.3 mAh g$^{-1}$ at a current density of 0.2 A g$^{-1}$. This capacity significantly surpasses those of several previously reported AZIB cathodes, including $VO_2$ (357 mAh g$^{-1}$) [32], $Na_{0.33}V_2O_5$ (367.1 mAh g$^{-1}$) [33], $Zn_2(OH)VO_4$ (204 mAh g$^{-1}$) [34], and other ammonium vanadate variants such as $(NH_4)_2V_4O_9$ (378 mAh g$^{-1}$) [35] and $(NH_4)_2V_6O_{16}$ (323.5 mAh g$^{-1}$) [36]. Remarkably, after 15 cycles, the NVO$_d$-3 cathode achieved a peak discharge capacity of 479.3 mAh g$^{-1}$. Moreover, after enduring 50 cycles, it maintained a capacity retention rate of approximately 90.1%, underscoring its exceptional durability and performance consistency in AZIBs applications.

Figure 5b–d present the galvanostatic charge-discharge profiles of NVO$_d$-2, NVO$_d$-3, and NVO$_d$-4, each tested at a current density of 0.2 A g$^{-1}$. Notably, all profiles feature two distinct, relatively flat charge-discharge plateaus, indicative of the complex electrochemical processes underway. These plateaus are attributed to the sequential reactions occurring within the NVO$_d$ electrode during the charge-discharge cycle, specifically the embedding and de-embedding of $Zn^{2+}$ ions coupled with the electron redox reactions.

Moreover, subsequent to the initial cycle, the profiles of these curves and their associated charge-discharge plateaus exhibit remarkable consistency across subsequent cycles, demonstrating a high degree of reproducibility with minimal deviation. Among the variants, NVO$_d$-4 exhibits the most pronounced curve overlap, albeit with the lowest discharge capacity. Conversely, NVO$_d$-2, while showing less pronounced curve overlap, achieves a slightly higher capacity than NVO$_d$-4. NVO$_d$-3 stands out by offering an optimal balance of high capacity and stability, showcasing its efficacy in maintaining performance across cycles. This observation underscores the critical interplay between

 doi:10.20944/preprints202402.1113.v1



structural integrity and electrochemical functionality within the $NVO_d$ materials, highlighting the nuanced impact of $O_d$ concentration on the overall performance of ammonium vanadate cathodes.

Figure 6a delineates the rate capabilities of $NVO_d$-2, $NVO_d$-3, and $NVO_d$-4 across a current density range from 0.1 to 10 A $g^{-1}$, while Figure 6b details the rate performance of pristine NVO within the same current density spectrum. Comparative analysis of the data presented in these figures reveals that $NVO_d$ variants manifest a significantly enhanced rate performance in comparison to pristine NVO. Notably, $NVO_d$-3 demonstrates remarkable capacities at varying current densities, achieving 476.4, 461.2, 427.8, 400.2, 340.8, 274.1, 188.7, and 148.7 mAh $g^{-1}$ at current densities of 0.1, 0.2, 0.5, 1, 3, 5, 8, and 10 A $g^{-1}$, respectively. In contrast, NVO exhibits capacities of 299.7, 294.4, 281.5, 250.4, 96.2, and 13.8 mAh $g^{-1}$ at 0.1, 0.2, 0.5, 1, 3, and 5 A $g^{-1}$, respectively, indicating a pronounced disparity in performance.

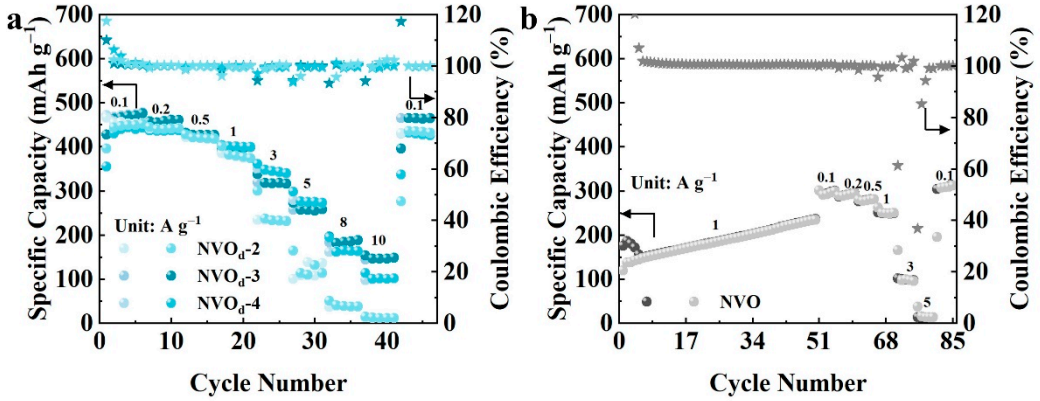


**Figure 6.** Rate performance of (**a**) $NVO_d$-2, $NVO_d$-3, $NVO_d$-4 and (**b**) NVO.

Both $NVO_d$-2 and $NVO_d$-4 display reversible specific capacities that are lower than those of $NVO_d$-3 at all tested current densities. Specifically, $NVO_d$-2 presents capacities of 449.3, 441.4, 420.1, 377.4, 233.2, 109.4, 38.1, and 12.3 mAh $g^{-1}$, while $NVO_d$-4 exhibits capacities of 449.1, 440.3, 420.1, 400.2, 343.3, 275.4, 165.4, and 101.3 mAh $g^{-1}$ at 0.1, 0.2, 0.5, 1, 3, 5, 8, and 10 A $g^{-1}$, respectively. Upon reverting the current density back to 0.1 A $g^{-1}$, all three materials demonstrate the ability to recover to their initial capacity values. Remarkably, the Zn//$NVO_d$-3 battery sustains a high capacity of 465.2 mAh $g^{-1}$ upon this return to the baseline current density, significantly outstripping the Zn//NVO, which registers a capacity of 304.2 mAh $g^{-1}$. The superior rate capability of $NVO_d$-3 underscores the beneficial impact of strategically introduced defects, which evidently enhance the kinetics of $Zn^{2+}$ embedding and de-embedding.s

Furthermore, long-term cycling performance of $NVO_d$-2, $NVO_d$-3, $NVO_d$-4, and pristine NVO was assessed, with the findings presented in Figure 7. These evaluations were conducted at a rigorous current density of 10 A $g^{-1}$ to test the endurance of the materials under high-rate conditions. Notably, $NVO_d$-3 initiated the test with an initial capacity of 198 mAh $g^{-1}$. This capacity observed a decrement during the initial cycles but reached a stable capacity of 169 mAh $g^{-1}$ after the first 10 cycles. Impressively, after 1500 cycles, $NVO_d$-3 maintained a capacity retention of 65.4% relative to its stabilized capacity, showcasing its durability and resilience over extended cycling.

 doi:10.20944/preprints202402.1113.v1



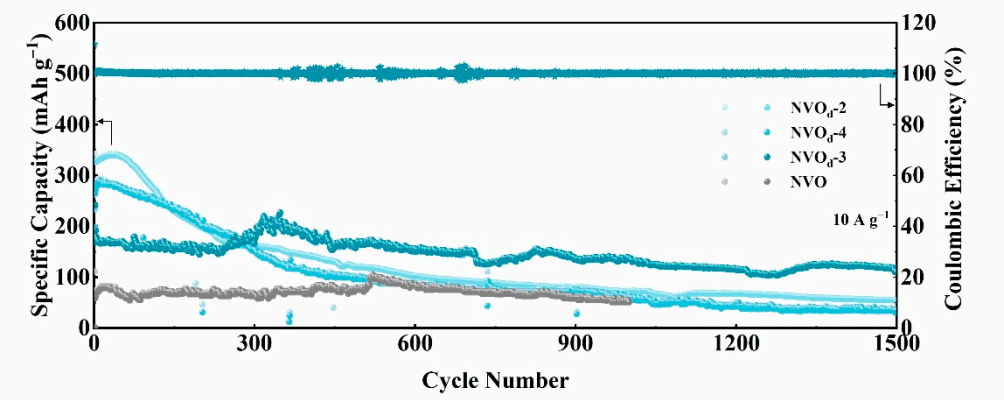


**Figure 7.** Cycling performance of $NVO_d$-2, $NVO_d$-3, $NVO_d$-4 and NVO at 10 A $g^{-1}$.

In contrast, pristine NVO started with an initial capacity of less than 100 mAh $g^{-1}$, underlining a significant disparity in performance when compared to the $NVO_d$ variants. While both $NVO_d$-2 and $NVO_d$-4 exhibited promising initial capacities exceeding 250 mAh $g^{-1}$, they suffered a precipitous decline to merely 30% of their initial capacities after 400 cycles, highlighting challenges in maintaining long-term stability. Among the materials tested, $NVO_d$-3 distinguished itself by demonstrating a commendable balance of high reversible specific capacity and sustained cycle stability.

To further investigate the electrochemical reaction mechanisms underpinning its performance, cyclic voltammetry (CV) tests were executed using an electrochemical workstation across a voltage window of 0.2 to 1.6 V, employing scan rates of 0.1, 0.2, 0.4, 0.6, and 0.8 mV $s^{-1}$, as depicted in Figure 8a,d,g. The CV results elucidate that an increase in the scan rate leads to enhanced polarization, which in turn precipitates a discernible shift in the oxidation and reduction peaks. Specifically, the oxidation peaks are observed to migrate towards higher voltages, while the reduction peaks shift towards lower voltages, indicating kinetic limitations within the electrochemical processes. Despite these shifts, the overall morphology of the CV curves remains consistent across the various scan rates.

The peak current density ($i$) and the scan rate ($v$) are governed by the following formulas, used to quantify the influence of capacitance and diffusion control on the overall capacitance:

$$i = av^b \quad (1)$$

$$log(i) = log(a) + blog(v) \quad (2)$$

$$i = k_1v + k_2v^{1/2} \quad (3)$$

Where the value of $b$ reflects the degree to which the electrochemical reaction is controlled by diffusion or capacitance. Generally, when $b$ approaches 0.5, it indicates a typical diffusion-controlled process, and when $b$ approaches 1, it suggests pseudocapacitive-dominated behavior. As shown in Figure 8b,e,h, the characteristic peak b values for $NVO_d$-2, $NVO_d$-3, and $NVO_d$-4 lie between 0.5 and 1, indicating contributions from both mechanisms, with pseudocapacitance playing a dominant role. Some peak values are largely influenced by capacitive control, approaching 1.

 doi:10.20944/preprints202402.1113.v1



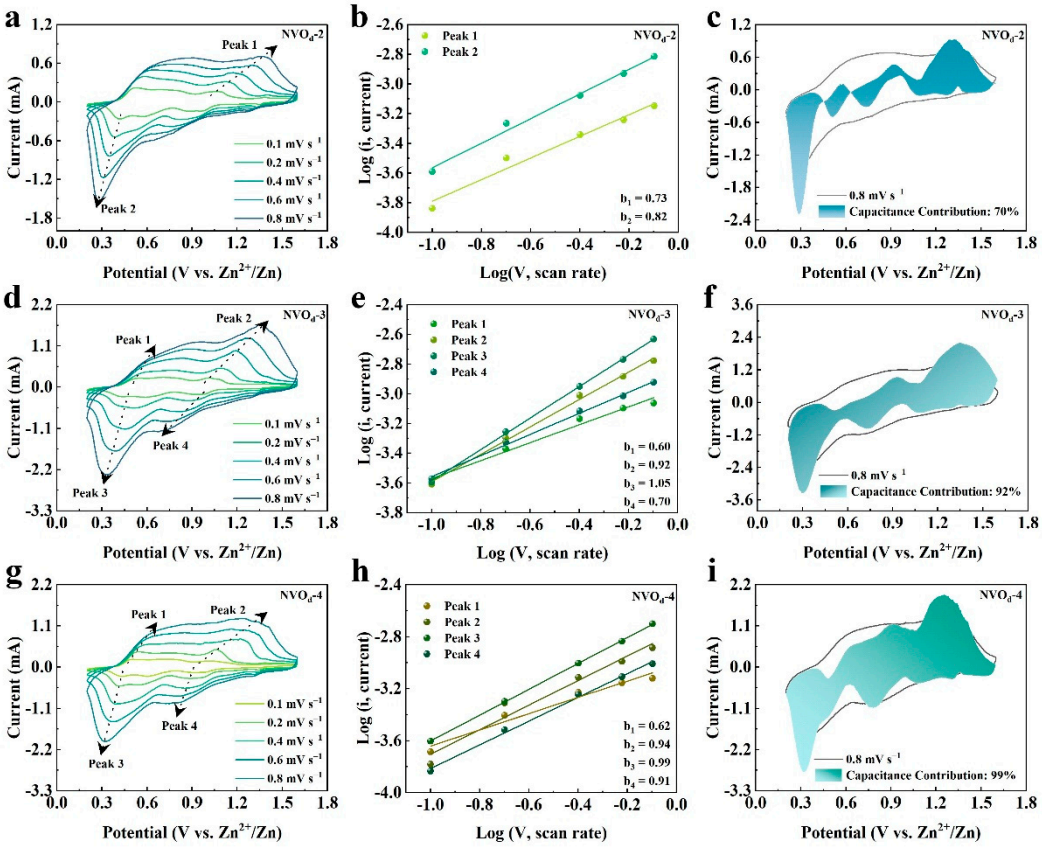


**Figure 8.** CV curves of electrode at different scan rates (**a**) NVO$_d$-2, (**d**) NVO$_d$-3, (**g**) NVO$_d$-4; The linear relationship between peak currents log($i$) and the square root of scan rates log($v$) (**b**) NVO$_d$-2, (**e**) NVO$_d$-3, (**h**) NVO$_d$-4; Pseudocapacitance contribution at 0.8 mV s$^{-1}$ (**c**) NVOd-2, (**f**) NVO$_d$-3, (**i**) NVO$_d$-4.

As delineated in Figure 8c,f,i, the analysis of pseudocapacitive contributions for NVO$_d$-2, NVO$_d$-3, and NVO$_d$-4 at a scan rate of 0.8 mV s$^{-1}$ reveals contribution rates of 70%, 92%, and 99%, respectively. Furthermore, Figure 9a,c,e showcases the variation in pseudocapacitive contribution rates of NVO$_d$-2, NVO$_d$-3, and NVO$_d$-4 across scan rates ranging from 0.1 to 0.8 mV s$^{-1}$. For NVO$_d$-2, the capacitive contribution escalates from 41% to 70%, for NVO$_d$-3, it increases from 79% to 92%, and for NVO$_d$-4, it advances from 91% to 99%. These observations underscore a distinct trend: with an increment in the concentration of oxygen defects, there is a corresponding increase in the pseudocapacitive contribution rate of the material.

The employment of the galvanostatic intermittent titration technique (GITT) provided further insight into the dynamics of $Zn^{2+}$ diffusion and its contribution to charge transfer within the material. The GITT experiments were performed at a controlled current density of 0.2 A g$^{-1}$, incorporating a relaxation period of 30 minutes and a data acquisition interval of 10 seconds. As illustrated in Figure 9b,d,f, the derived diffusion coefficients for $Zn^{2+}$ across the examined materials were found to range between $10^{-10}$ and $10^{-11}$ cm$^2$ s$^{-1}$, indicating a moderate diffusion rate conducive to electrochemical activity. Notably, the diffusion coefficient for NVO$_d$-3 was marginally superior compared to those of NVO$_d$-2 and NVO$_d$-4.

 doi:10.20944/preprints202402.1113.v1



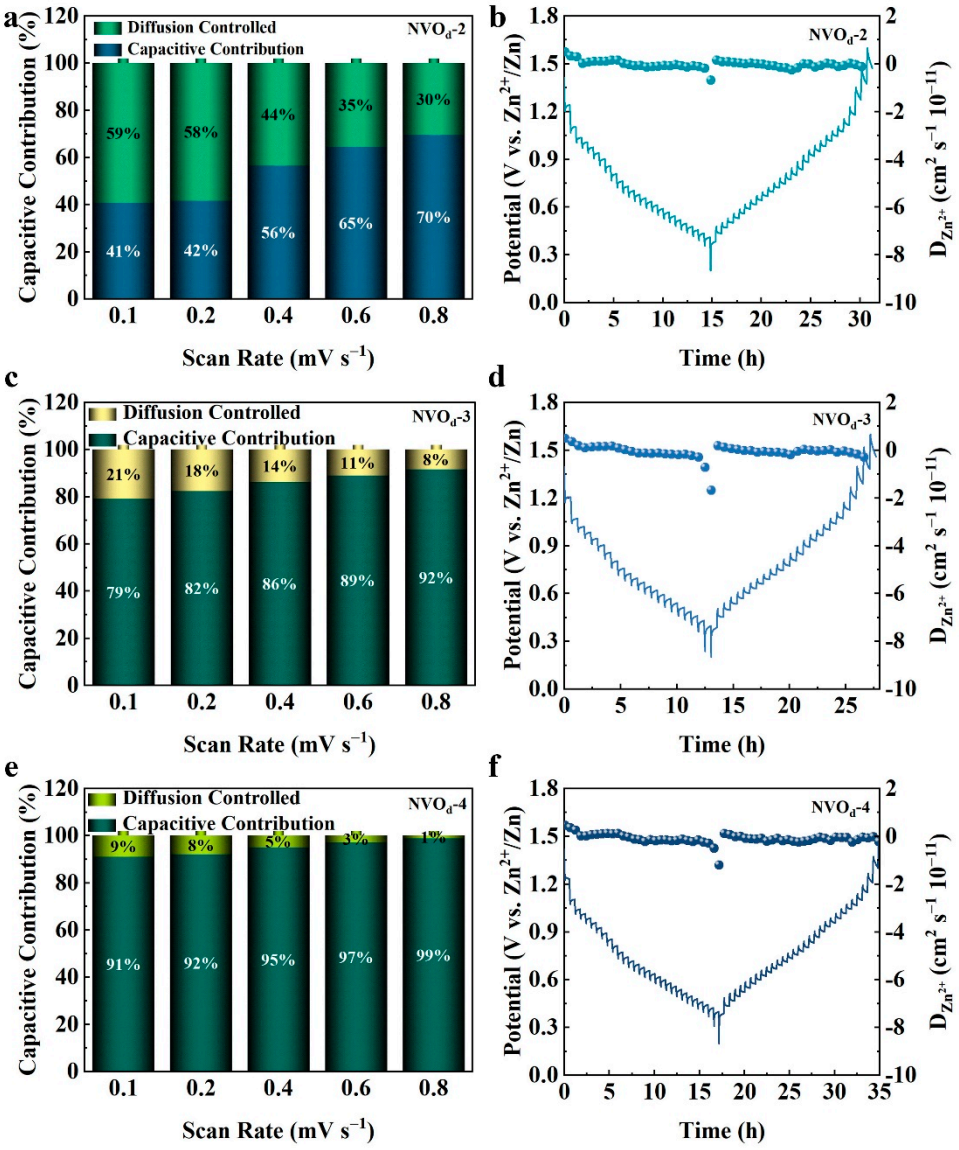


**Figure 9.** Capacitance contribution diagram at different scan rates (**a**) $NVO_d$-2, (**c**) $NVO_d$-3, (**e**) $NVO_d$-4; GITT diagram of (**b**) $NVO_d$-2, (**d**) $NVO_d$-3 and (**f**) $NVO_d$-4.

## 3. Materials and Methods

### *3.1. Calculation Method*

The DFT calculations were executed utilizing the Vienna Ab Initio Simulation Package (VASP) [37]. The Perdew–Burke–Ernzerhof (PBE) functional was employed to encapsulate the exchange-correlation interactions [38]. The computational approach incorporated a plane-wave basis set with an energy cutoff of 400 eV, paired with the Projector Augmented Wave (PAW) method [39,40]. Convergence thresholds for the self-consistent iterations and forces were set at $1\times10^{-5}$ eV and 0.01 eV $Å^{-1}$, respectively. The Brillouin zone was sampled using a 4×2×1 Γ-centered k-point mesh for the relaxation of the geometric structure and total energy calculations. For a more granular calculation of the density of states, an enhanced 8× 8×1 Γ-centered k-mesh was employed.

### *3.2. Preparation of Material*

Using a one-step water bath method, 0.468 g (4 mmol) of commercial $NH_4VO_3$ powder was dissolved in 50 mL of deionized water under a 70°C water bath. Once the reactant was fully dissolved, the solution turned pale yellow. Under stirring, thiourea of different molar amounts (2, 3, 4 mmol)

 doi:10.20944/preprints202402.1113.v1



was added. Subsequently, a certain amount of 0.1 M dilute hydrochloric acid was added dropwise to adjust the pH of the solution to approximately 2, followed by stirring for 30 minutes. The reaction continued for another 2 hours under a 90°C oil bath, yielding a dark green suspension. After naturally cooling to room temperature, the product was collected, washed with deionized water and ethanol, and dried in a 60°C vacuum oven for 24 hours to obtain the final oxygen-deficient $(NH_4)_2V_{10}O_{25}{\cdot}8H_2O$ nanoplates. These were respectively named as $NVO_d$-2 (2 mmol thiourea), $NVO_d$-3 (3 mmol thiourea), and $NVO_d$-4 (4 mmol thiourea). Under the same conditions, without adding any thiourea, NVO material was obtained.

### *3.3. Structure and Morphology Characterization*

XRD (Smart Lab SE) analyses were performed on the materials, employing Cu K$\alpha$ radiation, over a 2$\theta$ range of 5°–80°. To probe elemental valence changes within the materials, XPS (Thermo ESCALAB 250Xi) measurements were undertaken. To visualize the surface morphology, internal crystallography, and elemental dispersion of the samples, field emission SEM (Hitachi SU8010) was employed at ambient conditions. The existence of $O_d$ was ascertained through electron paramagnetic resonance spectroscopy (EMX nano).

### *3.4. Electrochemical Measurements*

In the fabrication of the tested cells, a CR2032-type button cell was employed as the model structure. The cells were assembled using Zn foil as the anode and titanium foil as the current collector, with filter paper serving as the separator. This assembly was conducted in an electrolytic environment comprising a 3 M $Zn(CF_3SO_3)_2$ solution, all under ambient conditions at room temperature. Electrochemical characterizations, including CV and EIS, were carried out on a CHI 760E electrochemical workstation, operating within a voltage window of 0.2 to 1.6 V. Furthermore, the LAND battery testing system was employed to critically assess the electrochemical behavior of the assembled cells in the study.

## 4. Conclusions

Guided by theoretical calculations, we have rationally designed $NVO_d$ nanosheets as a cathode material for aqueous AZIBs, which exhibit superior capacity and excellent cyclic performance. The genesis of the $O_d$ can be traced back to the incorporation of thiourea during the synthesis process. These $O_d$ play a pivotal role in modulating the internal structure of $NVO_d$, enhancing its conductivity, and thereby augmenting the electrochemical kinetics. Such improvements culminate in enhanced cyclic performance. Exploiting these attributes, the $NVO_d$-3 electrode we prepared demonstrated a remarkable capacity of 408 mAh $g^{-1}$ at a current density of 0.1 A $g^{-1}$, alongside outstanding stability across 1500 cycles with a capacity retention of 70.4%. Moreover, our findings reveal that the concentration of $O_d$ critically influences the pseudocapacitive contribution of the material. Specifically, the variant with the highest concentration of oxygen vacancies, $NVO_d$-4, showcases a pseudocapacitive contribution rate of 91% at a scan rate of 0.1 mV $s^{-1}$. These results underscore the significance of $O_d$ in the development of high-performance layered cathode materials for energy storage applications.

**Author Contributions:** Conceptualization, H.L. and X.C.; methodology, H.L. and Y.Z.; software, Y.Z.; validation, H.L., X.C. and Y.Z.; formal analysis, H.L. and X.C.; investigation, H.L., X.C. and Y.Z.; resources, X.C.; data curation, Y.Z.; writing—original draft preparation, H.L.; writing—review and editing, H.L., X.C. and Y.Z.; visualization, X.C. and Y.Z.; supervision, H.L.; project administration, H.L.; funding acquisition, H.L. All authors have read and agreed to the published version of the manuscript.

**Funding:** This research was funded by the National Natural Science Foundation of China, grant number 22065032, and Undergraduate Education and Teaching Research and Reform Project of Universities in Xinjiang Autonomous Region, grant number XJGXPTJG-202205. The APC was funded by High Level Overseas Educated Talents Returning to China Funding Candidate Program, grant number 2019160.

 doi:10.20944/preprints202402.1113.v1



**Data Availability Statement:** The data presented in this study are available on request from the corresponding author.

**Acknowledgments:** The authors acknowledge the shiyanjia lab (www. shiyanjia.com) for the TEM tests.

**Conflicts of Interest:** The authors declare no conflict of interest.

## References

1. Jia, X.; Liu, C.; Neale, Z.G.; Yang, J.; Cao, G. Active materials for aqueous zinc ion batteries: synthesis, crystal structure, morphology, and electrochemistry. *Chem. Rev.* **2020**, *120*, 7795–7866.
2. Zheng, Y.; Yao, Y.; Ou, J.; Li, M.; Luo, D.; Dou, H.; Li, Z.; Amine, K.; Yu, A.; Chen, Z. A review of composite solid-state electrolytes for lithium batteries: fundamentals, key materials and advanced structures. *Chem. Soc. Rev.* **2020**, *49*, 8790–8839.
3. Lin, X.; Khosravinia, K.; Hu, X.; Li, J.; Lu, W. Lithium plating mechanism, detection, and mitigation in lithium-ion batteries. *Prog. Energ. Combust.* **2021**, *87*, 100953.
4. Shadike, Z.; Tan, S.; Wang, Q.-C.; Lin, R.; Hu, E.; Qu, D.; Yang, X.-Q. Review on organosulfur materials for rechargeable lithium batteries. *Mater. Horiz.* **2021**, *8*, 471–500.
5. Selvakumaran, D.; Pan, A.; Liang, S.; Cao, G. A review on recent developments and challenges of cathode materials for rechargeable aqueous Zn-ion batteries. *J. Mater. Chem. A* **2019**, *7*, 18209–18236.
6. Zhang, N.; Wang, J.-C.; Guo, Y.-F.; Wang, P.-F.; Zhu, Y.-R.; Yi, T.-F. Insights on rational design and energy storage mechanism of Mn-based cathode materials towards high performance aqueous zinc-ion batteries. *Coordin. Chem. Rev.* **2023**, *479*, 215009.
7. Alfaruqi, M.H.; Mathew, V.; Gim, J.; Kim, S.; Song, J.; Baboo, J.P.; Choi, S.H.; Kim, J. Electrochemically induced structural transformation in a γ-$MnO_2$ cathode of a high capacity zinc-ion battery system. *Chem. Mater.* **2015**, *27*, 3609–3620.
8. Chen, D.; Lu, M.; Cai, D.; Yang, H.; Han, W. Recent advances in energy storage mechanism of aqueous zinc-ion batteries. *J. Energy. Chem.* **2021**, *54*, 712–726.
9. Wu, J.; Chi, X.; Liu, Y.; Yang, J.; Liu, Y. Electrochemical characterization of hollow urchin-like $MnO_2$ as high-performance cathode for aqueous zinc ion batteries. *J. Electroanal. Chem.* **2020**, *871*, 114242.
10. Mathew, V.; Sambandam, B.; Kim, S.; Kim, S.; Park, S.; Lee, S.; Alfaruqi, M.H.; Soundharrajan, V.; Islam, S.; Putro, D.Y.; Hwang, J.-Y.; Sun, Y.-K.; Kim, J. Manganese and vanadium oxide cathodes for aqueous rechargeable zinc-ion batteries: a focused view on performance, mechanism, and developments. *ACS Energy Lett.* **2020**, *5*, 2376–2400.
11. Sun, W.; Wang, F.; Hou, S.; Yang, C.; Fan, X.; Ma, Z.; Gao, T.; Han, F.; Hu, R.; Zhu, M.; Wang, C. Zn/$MnO_2$ battery chemistry with $H^+$ and $Zn^{2+}$ coinsertion. *J. Am. Chem. Soc.* **2017**, *139*, 9775–9778.
12. Yan, M.; He, P.; Chen, Y.; Wang, S.; Wei, Q.; Zhao, K.; Xu, X.; An, Q.; Shuang, Y.; Shao, Y.; Mueller, K.T.; Mai, L.; Liu, J.; Yang, J. Water-lubricated intercalation in $V_2O_5{\cdot}nH_2O$ for high-capacity and high-rate aqueous rechargeable zinc batteries. *Adv. Mater.* **2018**, *30*, 1703725.
13. Chen, D.; Lu, M.; Wang, B.; Cheng, H.; Yang, H.; Cai, D.; Han, W.; Fan, H.J. High-mass loading $V_3O_7{\cdot}H_2O$ nanoarray for Zn-ion battery: new synthesis and two-stage ion intercalation chemistry. *Nano Energy* **2021**, *83*, 105835.
14. Zhang, N.; Dong, Y.; Jia, M.; Bian, X.; Wang, Y.; Qiu, M.; Xu, J.; Liu, Y.; Jiao, L.; Cheng, F. Rechargeable aqueous Zn-$V_2O_5$ battery with high energy density and long cycle life. *ACS Energy Lett.* **2018**, *3*, 1366–1372.
15. Zhang, N.; Jia, M.; Dong, Y.; Wang, Y.; Xu, J.; Liu, Y.; Jiao, L.; Cheng, F. Hydrated layered vanadium oxide as a highly reversible cathode for rechargeable aqueous zinc batteries. *Adv. Funct. Mater.* **2019**, *29*, 1807331.
16. Zampardi, G.; Mantia, F.L. Prussian blue analogues as aqueous Zn-ion batteries electrodes: current challenges and future perspectives. *Curr. Opin. Electroche.* **2020**, *21*, 84–92.
17. Zhou, T.; Zhu, L.; Xie, L.; Han, Q.; Yang, X.; Chen, L.; Wang, G.; Cao, X. Cathode materials for aqueous zinc-ion batteries: a mini review. *J. Colloid. Interf. Sci.* **2022**, *605*, 828–850.
18. Zhang, L.; Chen, L.; Zhou, X.; Liu, Z. Towards high-voltage aqueous metal-ion batteries beyond 1.5 V: the zinc/zinc hexacyanoferrate system. *Adv. Energy Mater.* **2015**, *5*, 1400930.
19. Wu, X.; Qi, Y.; Hong, J.J.; Li, Z.; Hernandez, A.S.; Ji, X. Rocking-chair ammonium-ion battery: a highly reversible aqueous energy storage system. *Angew. Chem.Int. Edit.* **2017**, *56*, 13026–13030.
20. Konarov, A.; Voronina, N.; Jo, J.H.; Bakenov, Z.; Sun, Y.-K.; Myung, S.-T. Present and future perspective on electrode materials for rechargeable zinc-ion batteries. *ACS Energy Lett.* **2018**, *3*, 2620–2640.

 doi:10.20944/preprints202402.1113.v1




21. Kim, J.; Kim, J.H.; Ariga, K. Redox-active polymers for energy storage nanoarchitectonics. *Joule* **2017**, *1*, 739–768.
22. Kundu, D.; Oberholzer, P.; Glaros, C.; Bouzid, A.; Tervoort, E.; Pasquarello, A.; Niederberger, M. Organic cathode for aqueous Zn-ion batteries: taming a unique phase evolution toward stable electrochemical cycling. *Chem. Mater.* **2018**, *30*, 3874–3881.
23. Cui, H.; Ma, L.; Huang, Z.; Chen, Z.; Zhi, C. Organic materials-based cathode for zinc ion battery. *SmartMat* **2022**, *3*, 565–581.
24. Deng, Y.-P.; Liang, R.; Jiang, G.; Jiang, Y.; Yu, A.; Chen, Z. The current state of aqueous Zn-based rechargeable batteries. *ACS Energy Lett.* **2020**, *5*, 1665–1675.
25. Chen, L.; Ruan, Y.; Zhang, G.; Wei, Q.; Jiang, Y.; Xiong, T.; He, P.; Yang, W.; Yan, M.; An, Q.; Mai. L. Ultrastable and high-performance Zn/$VO_2$ battery based on a reversible single-phase reaction. *Chem. Mater.* **2019**, *31*, 699–706.
26. Shang, Y.; Kundu, D. Aqueous Zn-ion batteries: cathode materials and analysis. *Curr. Opin. Electroche.* **2022**, *33*, 100954.
27. Liu, Y.; Liu, Y.; Wu, X. Defect engineering of vanadium-based electrode materials for zinc ion battery. *Chinese Chem. Lett.* **2023**, *34*, 107839.
28. Lai, J.; Tang, H.; Zhu, X.; Wang, Y. A hydrated $NH_4V_3O_8$ nanobelt electrode for superior aqueous and quasi-solid-state zinc ion batteries. *J. Mater. Chem. A* **2019**, *7*, 23140–23148.
29. Wang, X.; Xi, B.; Feng, Z.; Chen, W.; Li, H.; Jia, Y.; Feng, J.; Qian, Y.; Xiong, S. Layered $(NH_4)_2V_6O_{16}\cdot 1.5H_2O$ nanobelts as a high-performance cathode for aqueous zinc-ion batteries. *J. Mater. Chem. A* **2019**, *7*, 19130–19139.
30. Liu, C.; Zhang, Y.; Cheng, H.; Cai, X.; Jia, D.; Lin, H. "Dual-engineering" strategy to regulate $NH_4V_4O_{10}$ as cathodes for high-performance aqueous zinc ion batteries. *Small* **2023**, *19*, 2301870.
31. Yan, M.; He, P.; Chen, Y.; Wang, S.; Wei, Q.; Zhao, K.; Xu, X.; An, Q.; Shuang, Y.; Shao, Y.; Mueller, K.T.; Mai, L.; Liu, J.; Yang, J. Introducing Ce ions and oxygen defects into $V_2O_5$ nanoribbons for efficient aqueous zinc ion storage. *Nano Res.* **2023**, *16*, 2445–2453.
32. Liu, N.; Wu, X.; Yin, Y.; Chen, A.; Zhao, C.; Guo, Z.; Fan, L.; Zhang, N. Constructing the efficient ion diffusion pathway by introducing oxygen defects in $Mn_2O_3$ for high-performance aqueous zinc-ion batteries. *ACS Appl. Mater. Interfaces* **2020**, *12*, 28199–28205.
33. Ding, J.; Du, Z.; Gu, L.; Li, B.; Wang, L.; Wang, S.; Gong, Y.; Yang, S. Ultrafast $Zn^{2+}$ intercalation and deintercalation in vanadium dioxide. *Adv. Mater.* **2018**, *30*, 1800762.
34. Ding, J.; Du, Z.; Gu, L.; Li, B.; Wang, L.; Wang, S.; Gong, Y.; Yang, S. A high-capacity and long-life aqueous rechargeable zinc battery using a metal oxide intercalation cathode. *Nat. Energy* **2016**, *1*, 16119.
35. Zhang, Y.; Jiang, H.; Xu, L.; Gao, Z.; Meng, C. Ammonium vanadium oxide $[(NH_4)_2V_4O_9]$ sheets for high capacity electrodes in aqueous zinc ion batteries. *ACS Appl. Energy Mater.* **2019**, *2*, 7861–7869.
36. Xu, L.; Zhang, Y.; Jiang, H.; Zheng, J.; Dong, X.; Hu, T.; Meng, C. Facile hydrothermal synthesis and electrochemical properties of (NH4)2V6O16 nanobelts for aqueous rechargeable zinc ion batteries. *Colloid. Surface. A* **2020**, *593*, 124621.
37. Kresse, G.; Furthmüller, J. Efficient iterative schemes for ab initio total-energy calculations using a plane-wave basis set. *Phys. Rev. B* **1996**, *54*, 11169–11186.
38. Perdew, J.P.; Burke, K.; Ernzerhof, M. Generalized gradient approximation made simple. *Phys. Rev. Lett.* **1996**, *77*, 3865–3868.
39. Kresse, G.; Joubert, D. From ultrasoft pseudopotentials to the projector augmented-wave method. *Phys. Rev. B* **1999**, *59*, 1758–1775.
40. Blöchl, P.E. Projector augmented-wave method. *Phys. Rev. B* **1994**, *50*, 17953–17979.